Article

Hot carriers from intra- and interband transitions in gold-silver alloy nanoparticles

Check for updates

Shreyas Ramachandran [1], Simão M. João [1], Hanwen Jin[1] & Johannes Lischner[1,2] ✉

Hot electrons and holes generated from the decay of localised surface plasmons in metallic nanoparticles can be harnessed for applications in solar energy conversion and sensing. In this paper, we study the generation of hot carriers in large spherical gold-silver alloy nanoparticles using a recently developed atomistic modelling approach that combines a solution of Maxwell's equations with large-scale tight-binding simulations. We find that hot-carrier properties depend sensitively on the alloy composition. Specifically, nanoparticles with a large gold fraction produce hot carriers under visible light illumination while nanoparticles with a large silver fraction require higher photon energies to produce hot carriers. Moreover, most hot carriers in nanoparticles with a large gold fraction originate from interband transitions which give rise to energetic holes and 'cold' electrons near the Fermi level. Increasing the silver fraction enhances the generation rate of hot carriers from intraband transitions which produce energetic electrons and 'cold' holes. These findings demonstrate that alloy composition is a powerful tuning parameter for the design of nanoparticles for applications in solar energy conversion and sensing that require precise control of hot-carrier properties.

Plasmonic nanoparticles (NPs) are an emerging platform for solar energy conversion devices, such as solar cells or photocatalysts. These systems feature large light absorption cross sections due to localised surface plasmons (LSPs) which are collective oscillations of the conduction electrons in the NP[1]. On the time scale of tens of femtoseconds, the LSP decays with the dominant decay channel being the Landau damping mechanism which results in the excitation of electron-hole pairs[2]. The excited carriers have large energies compared to the available thermal energy[3]. Such energetic or 'hot' carriers can be harnessed for a wide range of applications: for example, they can be used to drive chemical reactions[4,5], transferred to semiconductors for photovoltaic applications[6,7], or used for photodetection[8,9].

Nanoparticles composed of noble metals, such as Au[10–13] and Ag[10,13–16], have been studied intensively because of their favourable optical properties. However, pure metal NPs have some disadvantages: in particular, the LSP energy of Ag nanoparticles is quite high resulting in a small overlap with the solar spectrum. In contrast, Au NPs have a lower LSP energy, but a large fraction of the photoexcited carriers arises from interband transitions which do not generate energetic electrons that can be used for reduction reactions, such as CO_2 reduction. To overcome the limitations of the pure materials, several studies investigated the properties of noble metal alloys[17–24]. Because of the disorder in these systems, the rate of intraband transitions which give rise to energetic electrons is enhanced. This was exploited by Valenti and coworkers who demonstrated that Ag-Au alloy nanoparticles exhibit higher hot-electron injection efficiencies into the TiO_2 substrate compared to pure Au and Au nanoparticles[25]. Dahiya and coworkers prepared various Au-Cu alloys with tunable optical properties and higher catalytic turnover frequency than pure Au[26].

To accelerate the design of plasmonic alloy NPs for application in solar energy conversion devices, a detailed understanding of their electronic structure is required. However, application of standard electronic structure techniques, such as ab initio density-functional theory, to plasmonic NPs is challenging because of their large size containing thousands or even millions of atoms[2,27–30]. As a consequence, simplified electronic structure techniques, such as jellium or spherical well models, are often used to describe large NPs[31–33], but these techniques do not capture d-band derived NP states[34] or the dependence of electronic properties on the exposed NP facets[28]. To overcome these problems, Jin and coworkers recently introduced an atomistic electronic structure technique based on the tight-binding approach that allows the modelling

[1]Department of Materials, Imperial College London, London, UK. [2]The Thomas Young Centre for Theory and Simulation of Materials, London, UK. ✉e-mail: j.lischner@imperial.ac.uk

1

of hot-carrier generation in large NPs containing more than one million atoms[35]. They used this new approach to study the contributions to the hot-carrier generation rate from interband and intraband transitions in spherical NPs of Au, Ag and Cu[35] and also investigated hot-carrier generation in bi-metallic photocatalysts of Au and Pd[36].

In this paper, we study hot-carrier generation in Ag-Au alloy NPs using the atomistic modelling approach developed by Jin and coworkers[35]. We find that hot-carrier generation rates depend sensitively on the material composition and also on the photon energy. Specifically, a decrease in the Au fraction x_{Au} increases the LSP energy and also enhances the excitation rate of hot carriers generated from intraband transitions relative to the rate generated from interband transitions. Our results demonstrate that the alloy composition is an important tuning parameter for designing plasmonic NPs for solar energy conversion applications and our approach can be applied to other alloy systems in the future.

Results and discussion

Figure 1b shows the absorption cross sections of spherical Au-Au alloy nanoparticles of 20 nm diameter for a range of compositions $x_{Au} = (0.0, 0.2, 0.4, 0.6, 0.8, 1.0)$. For pure Ag nanoparticles (corresponding to $x_{Au} = 0.0$), the cross-section exhibits a sharp peak at the LSP energy of ~3.4 eV. Note that this peak lies outside the visible region and has a small overlap with the solar spectrum. Therefore, pure Ag NPs are not attractive for solar energy conversion devices, such as photocatalysts or solar cells. As the Ag content is reduced, the LSP energy decreases monotonically until the LSP energy of pure gold (~2.4 eV) is reached. As the Au content increases, the LSP moves into the visible region and the absorption cross-section has a larger overlap with the solar spectrum. Strikingly, the LSP peak of the alloy NPs is significantly smaller and broader than the Ag NP peak. These findings demonstrate the tunability of the optical properties of NPs by alloying.

Figure 2 shows the density of states (DOS) of spherical Ag-Au alloy nanoparticles (20 nm diameter corresponding to 246,857 atoms) for a range of compositions. In the alloy nanoparticles, Ag and Au atoms are randomly mixed and for each composition results are obtained by averaging over 100 disorder realisations. Example atomic structures of the alloy nanoparticles are shown in Fig. 1a. Below the Fermi energy, the DOS exhibits a prominent feature arising from d-band states. The onset of this d-band peak is at −1.9 eV for pure Au and at −3.0 eV for pure Ag. For the pure materials, the onset of the DOS is characterised by a sharp peak. In contrast, the alloy NPs do not exhibit such a sharp peak at the d-band onset. Such a broadening has also been observed in photoemission experiments of alloy nanoparticles[25]. The broadening is a consequence of the disorder that gives rise to scattering between the unperturbed states of the pure materials. This leads to a finite lifetime of the states which is reflected by an increase in their linewidths giving rise to a broader DOS.

Figure 3 shows the hot-carrier generation rates of the Ag-Au alloy nanoparticles for different photon energies ranging from 2.4 eV to 3.2 eV. Pure Au has a plasmon energy of 2.4 eV. Since this photon energy is larger than the d-band onset (relative to the Fermi level), the hot-carrier generation rate exhibits sharp peaks arising from interband transitions. Interband transitions give rise to energetic holes (peak near −2 eV), but the electrons are 'cold' (peak near the Fermi level). In addition, a smaller and broader peak arising from intraband transitions can be observed. Such transitions give rise to energetic electrons (peak near +2 eV), but cold holes (peak near the Fermi level). Increasing the photon energy leads to a reduction of the hot-carrier generation rates in pure Au since away from the plasmon resonance the field enhancement inside the NP is weaker. Interestingly, at a photon energy of 3.2 eV, the broad peaks arising from intraband transitions in the hot-carrier generation rates become very sharp. This happens because at this photon energy interband transition from the sp-band which crosses the Fermi level to a high-energy unoccupied band become possible, see Fig. 2 of the Supplementary Information for a band structure of bulk Au.

For an alloy NP with $x_{Au} = 0.8$, the largest hot-carrier generation rate is found at a photon energy of 2.6 eV corresponding to the LSP energy at this composition, see Fig. 1b. In comparison to the pure Au result, the hot-carrier generation rate of the alloy NP at the LSP energy is significantly reduced. This is a consequence of the smaller absorption cross section of alloy NPs. Interestingly, the alloy hot-carrier generation
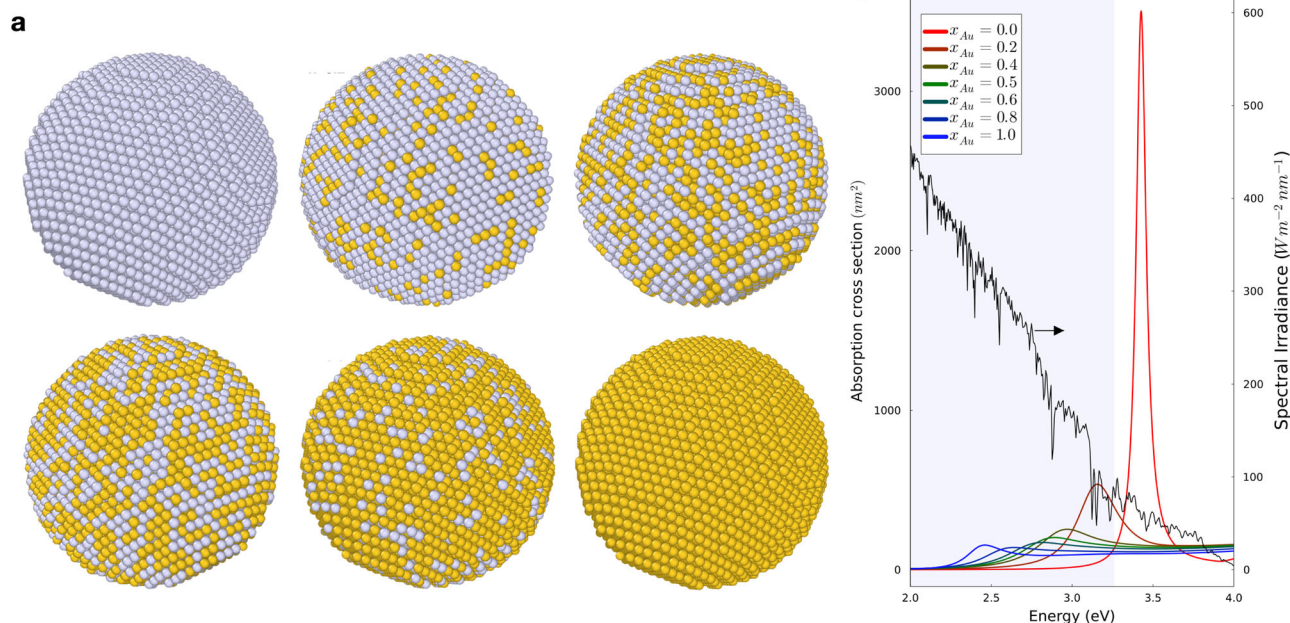
Fig. 1 | Atomic structures and absorption cross sections. a Atomic structures of spherical Au-Ag alloy nanoparticles of 20 nm diameter for Au fractions ranging from $x_{Au} = 0.0$ (top left) to $x_{Au} = 1.0$ (bottom right) in steps of $\Delta x_{Au} = 0.2$. Au atoms are yellow and Ag atoms are grey. **b** Absorption cross sections of spherical Au-Ag alloy nanoparticles of 20 nm diameter as a function of the NP composition. The solar irradiance (AM1.5 spectrum, credit to U.S. Department of Energy (DOE)/NREL/ALLIANCE) as a function of photon energy is shown in black with the visible region shaded in blue. The cross sections were calculated using the quasistatic approximation with experimentally measured bulk dielectric functions, see Methods section.

Fig. 2 | Normalised DOS for different spherical Au-Ag alloy nanoparticles of 20 nm diameter. The DOS is normalised to the total number of states available in the alloy NP ($9 \times N_{atoms}$). The different curves are offset by 0.065 eV for clarity and the Fermi level is set to 0 eV.
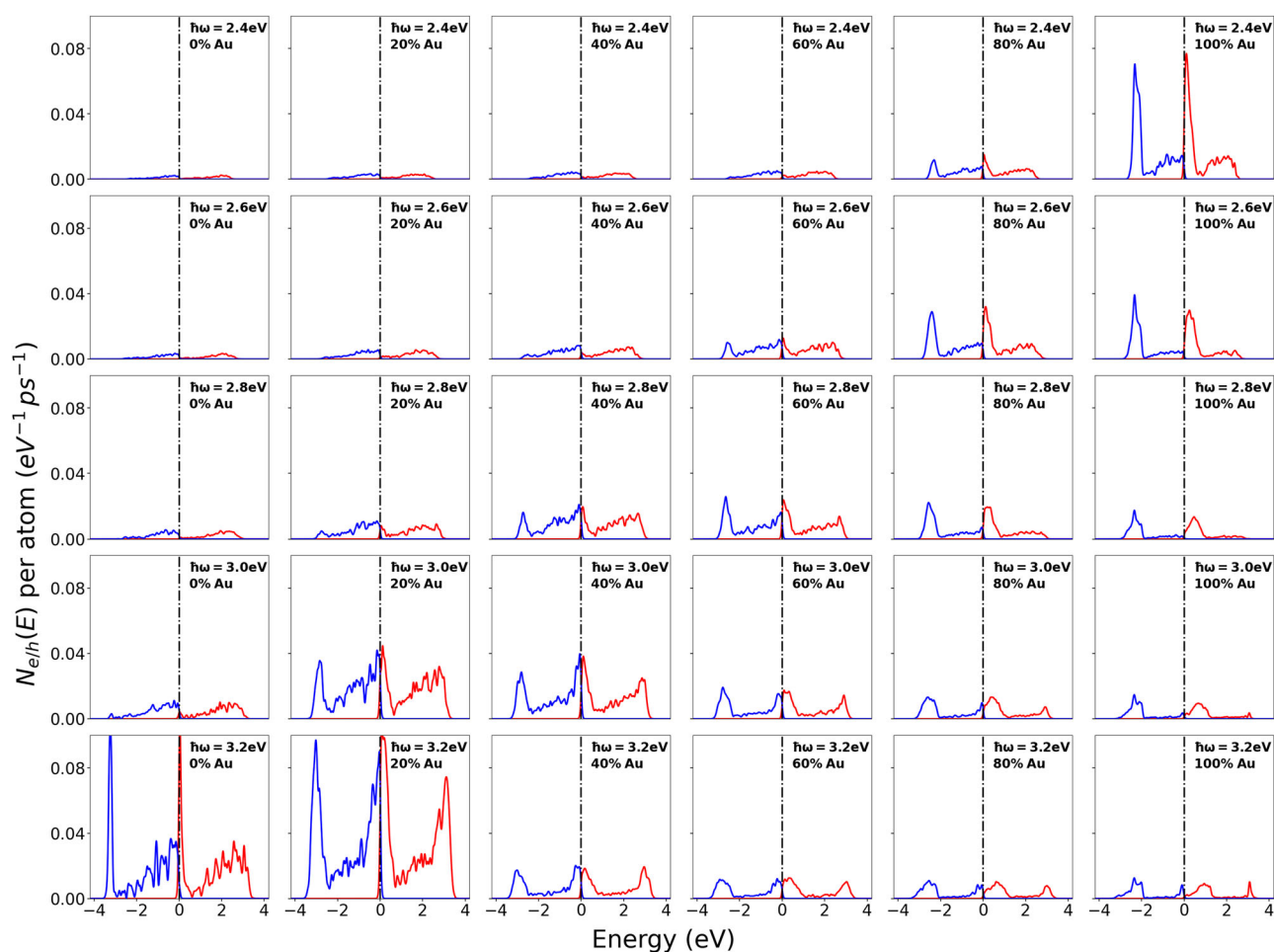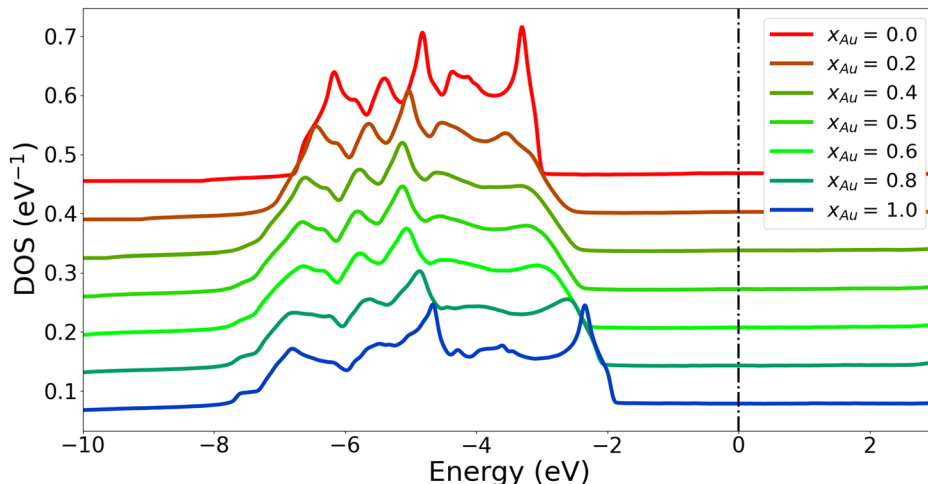

Fig. 3 | Hot-carrier generation rates for spherical Ag-Au alloy nanoparticles of 8 nm diameter as a function of alloy composition and photon energy. Hot-electron (hot-hole) generation rates are denoted by red (blue) lines. Each column corresponds to a fixed composition and each row to a fixed photon energy. The Fermi level is set to 0 eV.

rate at 2.6 eV has a larger intraband peak compared to the pure Au result at the same photon energy. Intraband transitions in a pure Au NP are only possible because the NP surface breaks translational invariance. In an alloy, disorder breaks translational invariance already in the bulk material and therefore no surface is required to excite intraband transitions. This demonstrates that the relative importance of interband and

intraband transitions for hot-carrier generation rates can be effectively controlled by tuning the alloy composition.

Further reduction of the Au content to $x_{Au} = 0.6$ completely suppresses the interband peak in the hot-carrier generation rates at small photon energies. This is a consequence of the shift and broadening of the d-band onset which make it increasingly difficult to excite interband transitions. For

Fig. 4 | Total hot-carrier generation rate per atom $N_{tot}(\omega)$ for spherical Ag-Au alloy nanoparticles as a function of photon energy and alloy composition $x_{\mathbf{Au}}$. The solar irradiance (AM1.5 spectrum) as a function of photon energy is shown in black.
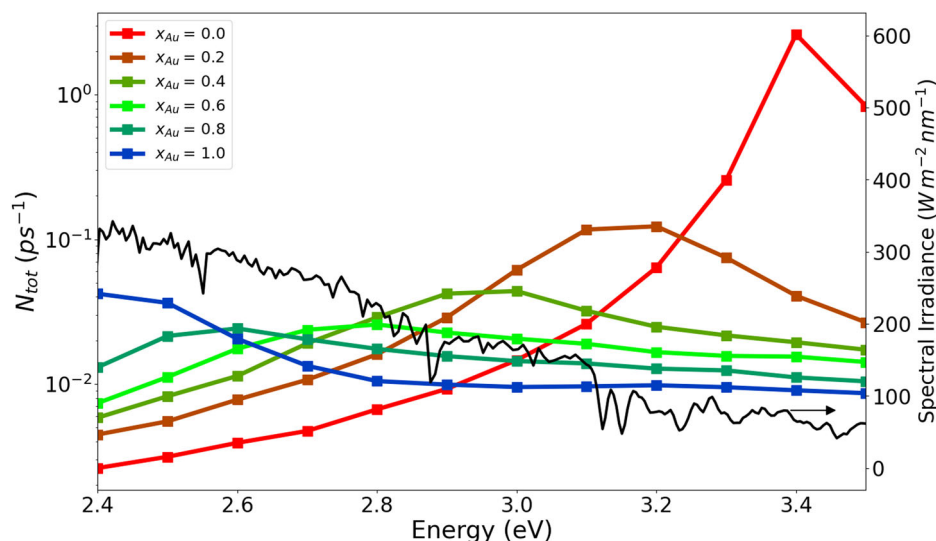
example, for NPs with $x_{Au} = 0.2$, the interband peaks are only observed for photon energies exceeding 2.8 eV.

Finally, pure Ag nanoparticles exhibit interband peaks only at photon energies larger than 3.1 eV. At photon energies closer to the LSP energy (3.4 eV for pure Ag), the hot-carrier generation rate is larger than that of pure Au nanoparticles. This is a consequence of the large absorption cross section of Ag nanoparticles, see Fig. 1b.

Figure 4 shows the total hot-carrier generation rate $N_{tot}(\omega)$ as function of alloy composition and photon energy. The largest generation rate is found for pure Ag NPs at their LSP energy of 3.4 eV. However, the overlap of the hot-carrier generation rate with the solar spectrum is small. The total hot-carrier generation rate of the alloy NPs is smaller and exhibits a broader peak than the pure Ag NP reflecting the behaviour of their absorption cross section. However, alloying increases the overlap of $N_{tot}(\omega)$ with the solar spectrum thus making alloy NPs more attractive for solar energy conversion applications.

Figure 5 compares the contributions from interband and intraband transitions to the total hot-carrier generation rate. Figure 5a, b show that pure Ag NPs exhibit the highest generation rate for hot carriers from both inter- and intraband transitions at the LSP energy. However, both contributions drop sharply as the photon energy is reduced. In contrast, the interband contribution in alloy NPs is relatively constant over a significant range of photon energies. Interestingly, the interband hot-carrier generation rate appears to only weakly depend on the alloy composition. The intraband contribution peaks at the LSP energy for each NP and shrinks as the Au content increases. Moreover, it can be seen that pure Au NPs produce more hot carriers from interband transitions than most alloy NPs, but most alloy NPs produce more hot carriers from intraband transitions than pure Au NPs. This happens because intraband transitions in pure Au nanoparticles can only occur near the surface which breaks translational invariance. In contrast, for alloy nanoparticles disorder breaks translational invariance already in the bulk material giving rise to additional intraband transitions and reducing the number of interband transitions. Finally, Fig. 5c shows the ratio of hot carriers generated from intraband transitions to the total generation rate. It can be observed that this ratio depends sensitively both on the photon energy and the alloy composition: for pure Au NPs, the ratio is relatively small (less than 0.4) and depends weakly on the photon energy. For pure Ag NPs, the ratio increases from 0.3 to 1.0 as the photon energy is reduced from 3.5 eV to 2.4 eV. Decreasing the Au content results in a significant increase in the intraband contribution. For example, NPs with $x_{Au} = 0.2$ and $x_{Au} = 0.4$ exhibit a dramatic increase compared to pure Au NPs in the relative contribution of hot carriers from intraband transitions at small photon energies.

Conclusion

In this work, we studied hot-carrier properties of alloys of Ag-Au alloy nanoparticles using an atomistic modelling technique that combines a solution of Maxwell's equations with large-scale tight-binding simulations. Specifically, we have calculated hot-carrier generation rates of large spherical nanoparticles for different compositions and photon energies. Our results demonstrate the hot-carrier generations depend sensitively on the alloy composition which controls both the optical and electronic properties of the nanoparticles: for example, the energy of the LSP depends on the material composition which in turn determines at which photon energy most hot carriers are generated. Moreover, the alloy composition determines the onset of d-band states relative to the Fermi level which in turn controls the photon energy at which interband transitions from d-band states to sp-band states become possible. Interband transitions produce energetic holes but 'cold' electrons near the Fermi level. To generate energetic electrons which can be harnessed for reduction reactions, the contribution of hot carriers from intraband transitions within the sp-band must be increased. This can be achieved by decreasing the Au content at fixed photon energy. Our findings demonstrate that the alloy composition is an important parameter which allows the continuous tuning of hot-carrier properties for specific applications in photocatalysis, photovoltaics or sensing. In the future, our approach can be applied to other alloy systems.

Methods

We calculate hot-carrier generation rates $N_e(E, \omega)$ (with E being the energy of the electrons and ω is the angular frequency of light) of spherical Au-Ag alloy nanoparticles following the approach developed by Jin and coworkers[35]. Using Fermi's golden rule, $N_e(E, \omega)$ can be expressed as

$$N_e(E, \omega) = \frac{2}{V} \sum_{if} \Gamma_{if}(\omega) \delta(E - E_f; \sigma), \qquad (1)$$

where i and f label initial and final states, respectively, V is the nanoparticle volume and the factor of 2 accounts for spin degeneracy. We define $\delta(x; \sigma) = \frac{1}{\sqrt{2\pi\sigma^2}} \exp(-\frac{x^2}{2\sigma^2})$ which becomes a delta function in the limit of $\sigma \to 0^+$ and $\sigma = 0.06$ eV is a broadening parameter. Finally, Γ_{if} is given by

$$\Gamma_{if}(\omega) = \frac{2\pi}{\hbar} |\langle \psi_f | \hat{\Phi}_{tot}(\omega) | \psi_i \rangle|^2 \delta(E_f - E_i - \hbar\omega; \sigma) f(E_i)(1 - f(E_f)), \quad (2)$$

where $f(E)$ denotes the Fermi-Dirac distribution evaluated at $T = 298$ K, $\hat{\Phi}_{tot}(\omega)$ is the total potential inside the nanoparticle. The total potential is calculated within the quasistatic approximation, i.e., we solve the Laplace equation $\nabla \cdot (\epsilon(\mathbf{r}, \omega) \nabla \Phi_{tot}(\mathbf{r}, \omega)) = 0$ for spherical nanoparticles with the
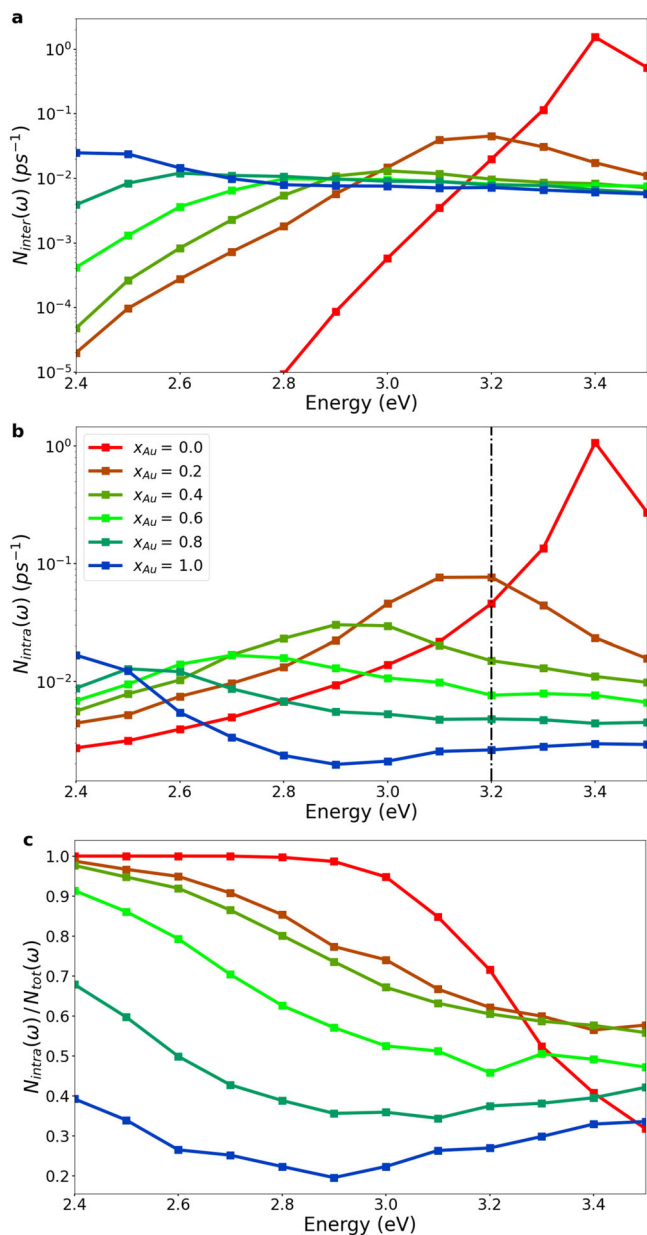
Fig. 5 | Different contributions to the hot carrier generation rate. Contribution to the total hot-carrier generation rate per atom from interband transitions (**a**) and intraband transitions (**b**) for spherical Ag-Au nanoparticles as a function of alloy composition x_{Au} and photon energy. **c** Ratio of intraband contribution to the total hot-carrier generation rate. The dashed vertical line in (**b**) indicates the energy at which interband transitions from the sp-band into the high-lying unoccupied band in pure Au become possible.

boundary condition at infinity $\Phi_{tot}(\mathbf{r}, \omega) = \Phi_{ext}(\mathbf{r}, \omega) = -E_0 z$. The analytical solution is given by

$$\Phi_{tot}(\mathbf{r}, \omega) = -eE_0 \frac{3\epsilon_m}{2\epsilon_m + \epsilon(\omega)} z. \qquad (3)$$

Here, $-e$ is the electron charge, $E_0 = 1$ V/nm, $\epsilon_m = 1$ is the dielectric constant of the environment and the dielectric function of the bulk alloy $\epsilon(\omega)$ is evaluated using the analytical model of Rioux and coworkers[37].

The hot-hole generation rate $N_h(E, \omega)$ is obtained by swapping the indices of the initial and final states in Eq. (1).

The electronic states of the alloy nanoparticles are obtained using a tight-binding (TB) model based on the work of ref. 38 that uses the valence

orbitals of Ag (4d, 5s, and 5p) and Au (5d, 6s, and 6p) as basis set. The interatomic matrix elements of the Hamiltonian are obtained using the two-centre Slater-Koster formalism[39]. The intra-atomic matrix elements describe the onsite energies E_{il} (where i labels an atom and $l = s, p, d$) which are expressed as

$$E_{il} = \varepsilon_{il} + \sum_{j \in NN_i} n_{ij} I_{ll\sigma}(R_{ij}), \qquad (4)$$

where ε_{il} is a constant and the second term on the right-hand side captures the variations of the onsite energies due to the chemical environment of atom i. Specifically, NN_i denotes the set of nearest neighbours of atom i, R_{ij} is the distance between atoms i and j, n_{ij} is the direction cosine between atoms i and j, and $I_{ll\sigma}$ is given by ref. 40

$$I_{ll\sigma}(R_{ij}) = I_{ll\sigma}^{(0)} \exp\left[-p_{ll\sigma} \left(\frac{R_{ij}}{R_{ij}^{(0)}} - 1 \right) \right], \qquad (5)$$

where $R_{ij}^{(0)}$ is the equilibrium distance between atoms i and j and $p_{ll\sigma}$ and $I_{ll\sigma}^{(0)}$ are fitting parameters.

The parameters of the tight-binding Hamiltonian for the Ag-Au alloy are taken from ref. 38. Note that in contrast to Hegde and coworkers, we do not take off-diagonal intra-atomic matrix elements into account since we have found that such matrix elements can give rise to unphysical results in nanoparticle calculations.

To construct the tight-binding Hamiltonian of a spherical Ag-Au nanoparticle of radius R, we start by setting up the Hamiltonian of a bulk alloy, choose an atom as the centre of the nanoparticle and then remove all inter- and intraatomic matrix elements involving atoms whose distance from the atom at the centre is larger than R. Note that in the procedure the onsite energies of atoms at the surface retain a bulk-like character.

To calculate the matrix element of the total potential, we use that

$$\langle j, \beta | \hat{\Phi}_{tot}(\omega) | i, \alpha \rangle = \left(-eE_0 \frac{3\epsilon_m}{2\epsilon_m + \epsilon(\omega)} z_j \right) \delta_{ij} \delta_{\alpha\beta}, \qquad (6)$$

where α and β label tight-binding basis functions and z_j denotes the z-coordinate of atom j.

Evaluating Eq. (1) is challenging for large nanoparticles since the calculation of the nanoparticle wavefunctions and energies requires a diagonalization of the tight-binding Hamiltonian. To avoid this, we use the kernel polynomial method, see refs. 35,41,42 for details. Additional details about implementation are provided in the Computational Details section in the Supplementary Information.

The total hot-electron generation rate (which is equal to the total hot-hole generation rate) is given by

$$N_{tot}(\omega) = \int_{E_f}^{\infty} N_e(E, \omega) dE, \qquad (7)$$

where E_f denotes the Fermi energy.

To determine the total number of holes (and electrons) $N_{inter}(\omega)$ generated by interband transitions, i.e., by a transition from a d-band state to an sp-band state, we first determine the d-band onset E_d from the nanoparticle DOS and then evaluate

$$N_{inter}(\omega) = \int_{-\infty}^{E_d} N_h(E, \omega) dE. \qquad (8)$$

To calculate the total number of electrons (and holes) $N_{intra}(\omega)$ generated from intra-band transitions, i.e., by a transition from an occupied

sp-band state to an empty sp-band state, we evaluate

$$N_{\text{intra}}(\omega) = \int_{E_d+\hbar\omega+\delta}^{\infty} N_e(E, \omega) dE \qquad (9)$$

with $\delta = 0.05$ eV chosen to exclude any contribution from interband transitions from d-bands to the sp-band. As discussed in the main text, at sufficiently high photon energies interband transitions from the sp-band which crosses the Fermi level to a high-energy unoccupied band become possible. Our approach does not allow us to separate these interband transitions from intraband transitions within the sp-band. For this reason, we also include these transitions into $N_{\text{intra}}(\omega)$.

Data availability
The data used for the findings in this study is available from the corresponding author upon reasonable request.

Code availability
The code used to generate the data in this study can be found on the public GitHub repository https://github.com/shreyas-ramachandran/nanoparticle-fgr.

References
1. Maier, S. A. *Plasmonics: Fundamentals and Applications* (Springer US, New York, NY, 2007). http://link.springer.com/10.1007/0-387-37825-1.
2. Brown, A. M., Sundararaman, R., Narang, P., Goddard, W. A. I. & Atwater, H. A. Nonradiative plasmon decay and hot carrier dynamics: effects of phonons, surfaces, and geometry. *ACS Nano* **10**, 957–966 (2016).
3. Narang, P., Sundararaman, R. & Atwater, H. A. Plasmonic hot carrier dynamics in solid-state and chemical systems for energy conversion. *Nanophotonics* **5**, 96–111 (2016).
4. Yan, L., Wang, F. & Meng, S. Quantum mode selectivity of plasmon-induced water splitting on gold nanoparticles. *ACS Nano* **10**, 5452–5458 (2016).
5. Mukherjee, S. et al. Hot electrons do the impossible: plasmon-induced dissociation of H2 on Au. *Nano Lett.* **13**, 240–247 (2013).
6. Takahashi, Y. & Tatsuma, T. Solid state photovoltaic cells based on localized surface plasmon-induced charge separation. *Appl. Phys. Lett.* **99**, 182110 (2011).
7. Enrichi, F., Quandt, A. & Righini, G. C. Plasmonic enhanced solar cells: summary of possible strategies and recent results. *Renew. Sustain. Energy Rev.* **82**, 2433–2439 (2018).
8. Tang, H. et al. Plasmonic hot electrons for sensing, photodetection, and solar energy applications: a perspective. *J. Chem. Phys.* **152**, 220901 (2020).
9. Sun, Q., Zhang, C., Shao, W. & Li, X. Photodetection by hot electrons or hot holes: a comparable study on physics and performances. *ACS Omega* **4**, 6020–6027 (2019).
10. Huynh, L. T. M., Kim, S. & Yoon, S. Effect of material and shape of nanoparticles on hot carrier generation. *ACS Photonics* **9**, 3260–3267 (2022).
11. Salmón-Gamboa, J. U. et al. Rational design of bimetallic photocatalysts based on plasmonically-derived hot carriers. *Nanoscale Adv.* **3**, 767–780 (2021).
12. Pensa, E. et al. Spectral screening of the energy of hot holes over a particle plasmon resonance. *Nano Lett.* **19**, 1867–1874 (2019).
13. Berdakin, M., Douglas-Gallardo, O. A. & Sánchez, C. G. Interplay between intra- and interband transitions associated with the plasmon-induced hot carrier generation process in silver and gold nanoclusters. *J. Phys. Chem. C.* **124**, 1631–1639 (2020).
14. Hoffmann, M. et al. Conjugated polymer-gold-silver hybrid nanoparticles for plasmonic energy focusing. *J. Phys. Chem. C.* **126**, 2475–2481 (2022).
15. Stefancu, A. et al. Fermi level equilibration at the metal-molecule interface in plasmonic systems. *Nano Lett.* **21**, 6592–6599 (2021).
16. Seemala, B. et al. Plasmon-mediated catalytic O2 dissociation on Ag nanostructures: hot electrons or near fields? *ACS Energy Lett.* **4**, 1803–1809 (2019).
17. Cortie, M. B. & McDonagh, A. M. Synthesis and optical properties of hybrid and alloy plasmonic nanoparticles. *Chem. Rev.* **111**, 3713–3735 (2011).
18. Link, S., Wang, Z. L. & El-Sayed, M. A. Alloy formation of gold-silver nanoparticles and the dependence of the plasmon absorption on their composition. *J. Phys. Chem. B* **103**, 3529–3533 (1999).
19. Blaber, M. G., Arnold, M. D. & Ford, M. J. A review of the optical properties of alloys and intermetallics for plasmonics. *J. Phys.: Condens. Matter* **22**, 143201 (2010).
20. Jawad, M. et al. Plasmonic effects and size relation of gold-platinum alloy nanoparticles. *Adv. Nano Res.* **7**, 169–180 (2019).
21. Darmadi, I., Khairunnisa, S. Z., Tomeček, D. & Langhammer, C. Optimization of the composition of PdAuCu ternary alloy nanoparticles for plasmonic hydrogen sensing. *ACS Appl. Nano Mater.* **4**, 8716–8722 (2021).
22. Bhatia, P., Verma, S. S. & Sinha, M. M. Tunable optical properties of Ni-Ag and Ni-Au nanoparticles in magneto-plasmonic nanostructures. *Optical Quantum Electron.* **52**, 473 (2020).
23. Coviello, V., Forrer, D. & Amendola, V. Recent developments in plasmonic alloy nanoparticles: synthesis, modelling, properties and applications. *ChemPhysChem* **23**, e202200136 (2022).
24. Gong, C. & Leite, M. S. Noble metal alloys for plasmonics. *ACS Photonics* **3**, 507–513 (2016).
25. Valenti, M. et al. Hot carrier generation and extraction of plasmonic alloy nanoparticles. *ACS Photonics* **4**, 1146–1152 (2017).
26. Dahiya, A., Verma, M. & Kumar, P. S. Plasmonic applications of gold-copper bimetallic alloy nanoparticles. *Plasmonics* **17**, 2173–2186 (2022).
27. Fojt, J., Rossi, T. P., Kumar, P. V. & Erhart, P. Tailoring hot-carrier distributions of plasmonic nanostructures through surface alloying. *ACS Nano* **18**, 6398–6405 (2024).
28. Rossi, T. P., Erhart, P. & Kuisma, M. Hot-carrier generation in plasmonic nanoparticles: the importance of atomic structure. *ACS Nano* **14**, 9963–9971 (2020).
29. Fojt, J., Rossi, T. P., Kuisma, M. & Erhart, P. Hot-carrier transfer across a nanoparticle-molecule junction: the importance of orbital hybridization and level alignment. *Nano Lett.* **22**, 8786–8792 (2022).
30. Kumar, P. V. et al. Plasmon-induced direct hot-carrier transfer at metal-acceptor interfaces. *ACS Nano* **13**, 3188–3195 (2019).
31. Manjavacas, A., Liu, J. G., Kulkarni, V. & Nordlander, P. Plasmon-induced hot carriers in metallic nanoparticles. *ACS Nano* **8**, 7630–7638 (2014).
32. Román Castellanos, L., Hess, O. & Lischner, J. Dielectric engineering of hot-carrier generation by quantized plasmons in embedded silver nanoparticles. *J. Phys. Chem. C.* **125**, 3081–3087 (2021).
33. Román Castellanos, L., Kahk, J. M., Hess, O. & Lischner, J. Generation of plasmonic hot carriers from d-bands in metallic nanoparticles. *J. Chem. Phys.* **152**, 104111 (2020).
34. Tagliabue, G. et al. Ultrafast hot-hole injection modifies hot-electron dynamics in Au/p-GaN heterostructures. *Nat. Mater.* **19**, 1312–1318 (2020).
35. Jin, H., Kahk, J. M., Papaconstantopoulos, D. A., Ferreira, A. & Lischner, J. Plasmon-induced hot carriers from interband and intraband transitions in large noble metal nanoparticles. *PRX Energy* **1**, 013006 (2022).

36. Jin, H., Herran, M., Cortes, E. & Lischner, J. Theory of hot-carrier generation in bimetallic plasmonic catalysts. *ACS Photonics* **10**, 3629–3636 (2023).

37. Rioux, D. et al. An analytic model for the dielectric function of Au, Ag, and their alloys. *Adv. Opt. Mater.* **2**, 176–182 (2014).

38. Hegde, G., Povolotskyi, M., Kubis, T., Boykin, T. & Klimeck, G. An environment-dependent semi-empirical tight binding model suitable for electron transport in bulk metals, metal alloys, metallic interfaces, and metallic nanostructures. I. Model and validation. *J. Appl. Phys.* **115**, 123703 (2014).

39. Slater, J. C. & Koster, G. F. Simplified LCAO method for the periodic potential problem. *Phys. Rev.* **94**, 1498–1524 (1954).

40. Harrison, W. A. *Electronic Structure and the Properties of Solids: The Physics of the Chemical Bond* (Dover Publications, 2012).

41. Weiße, A., Wellein, G., Alvermann, A. & Fehske, H. The kernel polynomial method. *Rev. Mod. Phys.* **78**, 275–306 (2006).

42. Jackson, D. *Über die Genauigkeit der Annäherung stetiger Funktionen durch ganze rationale Funktionen gegebenen Grades und trigonometrische Summen gegebener Ordnung* (Dieterich, Göttingen, 1911). https://gdz.sub.uni-goettingen.de/id/PPN30230648X.

Author contributions
H.J. and S.M.J. wrote the code, S.R. modified the code and performed the simulations. All authors contributed to the data analysis equally. J.L. supervised the work.

Competing interests
The authors declare no competing interests.

Additional information
Supplementary information The online version contains supplementary material available at https://doi.org/10.1038/s42004-024-01244-w.

Correspondence and requests for materials should be addressed to Johannes Lischner.

Peer review information *Communications Chemistry* thanks Wei-Shun Chang, Tarak Karmakar and the other, anonymous, reviewer(s) for their contribution to the peer review of this work.

Reprints and permissions information is available at http://www.nature.com/reprints

Publisher's note Springer Nature remains neutral with regard to jurisdictional claims in published maps and institutional affiliations.